

# The First Selected Configuration Interaction Implementation with Distributed Storage of the Configuration Interaction Vector

Enhua Xu,<sup>\*</sup> William Dawson, and Takahito Nakajima

*RIKEN Center for Computational Science, Kobe, Japan*

E-mail: enhua.xu@riken.jp

## Abstract

In recent years, the hybrid “QC+HPC” strategy—where quantum computers screen important determinants, followed by exact diagonalization on classical computers—has shown great potential in the study of strongly correlated systems in quantum chemistry. Last year, an IBM team proposed a novel scheme that utilizes quantum computers to select important bitstrings, which are then used to construct a spin-adapted determinant space via tensor products. In this work, we have specifically designed an entirely new algorithm for this tensor-product bitstring selected configuration interaction (SCI). For the first time worldwide, we have implemented distributed storage of the configuration interaction (CI) vector in this SCI framework, enabling massively parallel execution and scalable treatment of trillion-determinant spaces. Since this study is independent and does not involve determinant selection by quantum computers, we demonstrate our implementation’s capabilities by performing large-scale full configuration interaction (FCI) computations on the supercomputer Fugaku. The largest case is N<sub>2</sub> (cc-pVTZ) under D<sub>2h</sub> symmetry, involving  $2.62 \times 10^{12}$  determinants after freezing the core orbitals.

This scale surpasses the previous SCI record ( $2 \times 10^9$  determinants) by over three orders of magnitude, and even doubles the size of the largest FCI calculation reported to date ( $1.31 \times 10^{12}$  determinants). Remarkably, this result was achieved within the SCI framework, yet it exceeds the largest known full CI calculation. This work sets a new benchmark for SCI implementations and provides a scalable and efficient framework that can be extended to a wide range of SCI methodologies.

## 1 Introduction

Full Configuration Interaction (FCI) is an exact method for solving the Schrödinger equation in quantum chemistry.<sup>1-5</sup> However, due to its exponential scaling with system size, FCI remains limited to small molecules with small basis sets. Enabled by distributed storage of the configuration interaction (CI) vector,<sup>2</sup> as of 2024 FCI implementations have reached a scale of  $1.31 \times 10^{12}$  determinants.<sup>5</sup>

In practical applications, the coupled cluster singles and doubles with perturbative triples [CCSD(T)] method<sup>6</sup> is widely regarded as the gold standard for weakly correlated systems, owing to its balanced accuracy and efficiency. In contrast, accurately describing strongly correlated systems remains one of the most formidable challenges in quantum chemistry. The selected configuration interaction (SCI) method has long been employed and is recognized as one of the most promising methods for addressing this issue. Over the past decades, several SCI methods have been proposed and developed, such as the Configuration Interaction using a Perturbative Selection made Iteratively (CIPSI),<sup>7</sup> Adaptive Sampling CI (ASCI),<sup>8,9</sup> Semistochastic Heat-Bath CI (SHCI),<sup>10-12</sup> and iterative CI (iCI).<sup>13-15</sup> While distributed storage of the CI vector has been successfully applied in FCI calculations,<sup>2,3,5</sup> its implementation in SCI poses significant challenges due to the irregular and dynamically evolving nature of the determinant space. To date, all existing SCI implementations have employed replicated CI vectors, which imposes a strict memory limit on the maximum feasible CI vector size, even when multiple nodes are used. As a consequence, the largest SCI calculation reported

to date contains just  $2 \times 10^9$  determinants, far smaller than the  $1.31 \times 10^{12}$  determinants achieved in state-of-the-art FCI computations.

Meanwhile, rapid progress in quantum computing (QC) has led several research groups to explore hybrid approaches that combine quantum and classical computers for studying strongly correlated systems. In 2023, QunaSys first proposed a strategy that uses quantum computers to screen important Slater determinants, followed by exact diagonalization on classical computers—a method referred to as Quantum-Selected Configuration Interaction (QSCI).<sup>16</sup> A downside to this approach is that the noise in quantum computers may cause some determinants to be missed, making the wavefunction deviate from the eigenstates of the  $\hat{S}^2$  operator. To overcome this issue, in 2024 an IBM team proposed an extension of the QSCI strategy in which quantum computers are used to select important bitstrings, after which the complete determinants are constructed via tensor products of the selected bitstrings.<sup>17</sup> In this paper, we refer to this approach as Tensor-Product Bitstring SCI (TBSCI), as it is based on the tensor product structure of  $\alpha$  and  $\beta$  bitstrings.

In this work, we have, for the first time worldwide, implemented distributed storage of the CI vector in an SCI program, overcoming single-node memory limitation and enabling the use of the entire supercomputer’s available memory for larger-scale calculations. Moreover, we have designed an entirely new, highly efficient algorithm specifically for TBSCI, leveraging its unique tensor-product structure, and further optimized the program for efficient parallel execution on the supercomputer Fugaku. We also validate the use of single precision to reduce computational cost and memory use; this is a strategy pursued for Configuration Interaction as early as the work of Pakiari and Handy,<sup>18</sup> and in line with current trends in correlated methods.<sup>19</sup> The combination of low memory footprint and low precision operations make our work promising for application to leadership class supercomputers based on GPUs.

Ultimately, we have used our implementation to compute: the potential energy surfaces (PESs) of  $N_2$  (aug-cc-pVDZ) and CN (cc-pVTZ), as well as single-point energies of  $Cr_2$  (STO-3G) and  $N_2$  (cc-pVTZ) near their equilibrium geometries. Among these systems, the

largest case is  $\text{N}_2$  (cc-pVTZ), involving  $2.62 \times 10^{12}$  determinants under  $D_{2h}$  symmetry with the frozen-core approximation. This scale surpasses the previous SCI record of  $2 \times 10^9$  determinants<sup>12</sup> by more than three orders of magnitude, and even doubles the size of the largest FCI calculation reported to date ( $1.31 \times 10^{12}$  determinants).<sup>5</sup>

At present, our work focuses on implementing distributed storage of the CI vector in the Davidson diagonalization step of SCI—a particularly challenging component in the development of large-scale SCI methods. The subsequent second-order perturbative correction on top of SCI has not yet been implemented in such a distributed manner. As a result, our current program cannot perform a complete SCI calculation. Instead, we demonstrate its capabilities by performing FCI calculations, the results of which can serve as valuable benchmark data for future research in quantum chemistry.

## 2 A Novel and Highly Efficient Algorithm for TBSCI

In this section, we describe a novel and highly efficient algorithm specifically designed for TBSCI, which combines distributed storage of the CI vector with a suite of MPI optimization strategies to enable trillion-scale determinant calculations on modern supercomputers.

### 2.1 Distributed Storage of CI Vector

In the general framework of TBSCI, the sets of the selected bitstrings can be defined as  $\{S_w^\alpha \mid w = 1, 2, \dots, l_\alpha\}$  and  $\{S_u^\beta \mid u = 1, 2, \dots, l_\beta\}$ , where  $\{S^\alpha\}$  and  $\{S^\beta\}$  are the sets of selected  $\alpha$ -spin and  $\beta$ -spin bitstrings, respectively, with elements denoted as  $S_w^\alpha$  and  $S_u^\beta$ . Here,  $l_\alpha$  denotes the number of selected  $\alpha$  and  $l_\beta$  the number of selected  $\beta$  bitstrings. The determinant space constructed via tensor products is then given by:

$$\{|S_w^\alpha\rangle \otimes |S_u^\beta\rangle \mid w = 1, \dots, l_\alpha; u = 1, \dots, l_\beta\}. \quad (1)$$

The ordering of  $\{S^\alpha\}$  and  $\{S^\beta\}$  can be freely chosen. However, once determined, the index order of the determinants in the determinant space is also fixed. Specifically, the  $K$ -th determinant is denoted as  $|D_K\rangle$  and given by:

$$|D_K\rangle = |S_w^\alpha\rangle \otimes |S_u^\beta\rangle, \quad w = \frac{K}{l_\beta} + 1, \quad u = \text{MOD}(K, l_\beta). \quad (2)$$

For convenience,  $|D_K\rangle$  will be denoted as  $|D_{(w,u)}\rangle$  throughout this work.

When the number of determinants exceeds the storage capacity of a single node, the CI vector must be distributed across nodes. In this work, the term CI vector refers to the array of CI coefficients stored in the same order as the determinant indices. As illustrated in Fig. 1, we distribute the determinants based on their  $\alpha$  bitstrings while ensuring an approximately even allocation, a strategy known as memory balance.

Since the determinants are indexed such that  $\alpha$  bitstrings vary first, followed by  $\beta$  bitstrings, we define a *segment* as the subset of the CI vector corresponding to all determinants sharing the same  $\alpha$  bitstring. In this work, we denote the total number of processes (each node runs exactly one process) as  $N$ . Let  $m_p$  denote the number of  $\alpha$  bitstrings assigned to process  $p$  (where  $p = 0, 1, \dots, N - 1$ ), with  $\sum_{p=0}^{N-1} m_p = l_\alpha$ . Then, each process contains  $m_p$  segments and thus is responsible for a total of  $m_p \times l_\beta$  determinants. As each determinant is fully defined by its index through Eq. (2), our program does not require additional memory to store determinant composition information.

## 2.2 Distributed Matrix-Vector Multiplication

In this work, we employ the traditional Davidson diagonalization method<sup>20</sup> for CI calculations, where the core computational step is evaluating  $\mathbf{W} = H \cdot \mathbf{U}$ , with Hamiltonian matrix  $H$ , and CI vectors  $\mathbf{W}$  and  $\mathbf{U}$ .

The most advanced SCI implementations to date follow two main strategies: some store the nonzero Hamiltonian elements in a distributed manner across nodes (e.g., DICE<sup>12</sup>), while

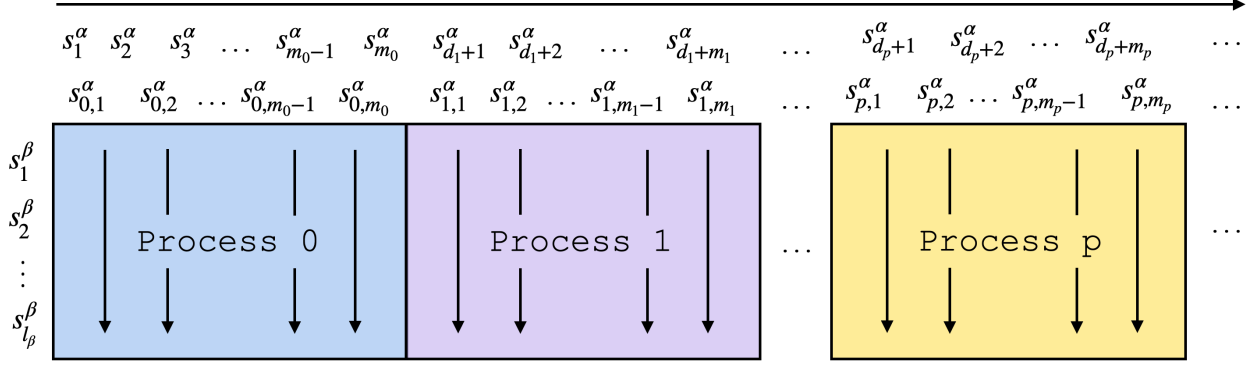


Figure 1: Distribution of the CI vector into segments across  $N$  processes. Each process holds a strict subset of  $m_p$   $\alpha$  strings. On a local process, the determinants are divided into segments (represented by vertical arrows), where a segment is composed of all determinants that share the same  $\alpha$  string. For this figure, we define a displacement index  $d_p = \sum_{i=0}^{p-1} m_i$  to show the offset of  $\alpha$  strings on a given process.

others compute the Hamiltonian matrix elements on-the-fly (e.g., `QUANTUM`<sup>21</sup>). However, both approaches store the CI vector entirely on a single node without exception. The advantage of these approaches is that each computing node performs a simple matrix-vector multiplication; at the end of each Davidson iteration, the effective Hamiltonian matrix can be efficiently constructed using an `MPI_ALLREDUCE` operation. However, a key limitation is that the CI vector size is strictly constrained by the memory of a single node, posing a major bottleneck in utilizing supercomputing resources for larger determinant spaces.

In our program, the CI vector is distributed across MPI processes, with exactly one process running on each node. In this setting, each node  $p$  only stores its corresponding CI vector segments. The computation of  $\mathbf{W}_p$  is then given by:

$$\mathbf{W}_p = \sum_q H \cdot \mathbf{U}_q. \quad (3)$$

This implies that, in a single Davidson iteration, node  $p$  theoretically needs to sequentially fetch data from all other nodes to compute  $\mathbf{W}_p$ . We define each individual fetch-and-compute operation (i.e., computing  $\mathbf{W}_p += H \cdot \mathbf{U}_q$ ) as one *step*. Since there are  $N$  computing nodes, each Davidson iteration consists of  $N$  steps. Unlike the implementation in `QUANTUM`, we

precompute and store the diagonal elements of the Hamiltonian matrix across processes in a distributed manner consistent with the CI vector, while the off-diagonal elements are computed on-the-fly during the Davidson iterations.

During the  $N$  computation steps within a single Davidson iteration, each node operates independently without global synchronization. For example, once node  $p$  completes the computation  $\mathbf{W}_p += H \cdot \mathbf{U}_q$ , it immediately fetches  $\mathbf{U}_r$  from node  $r$  and proceeds with  $\mathbf{W}_p += H \cdot \mathbf{U}_r$ . This design is crucial because computation times vary across different steps and nodes. Enforcing synchronization after each step would lead to unnecessary waiting and degrade computational efficiency. For data communication, we adopt the `MPI_GET` operation, a type of one-sided communication, allowing nodes to fetch data asynchronously without interrupting the computation on the target node, further improving efficiency.

## 2.3 Efficient Hamiltonian Computation for TBSCI

Due to the Slater-Condon rules,  $H$  is a highly sparse matrix, so minimizing operations that involve zero elements is crucial for efficiency. In the DICE program, the nonzero Hamiltonian elements are precomputed and stored in a distributed manner along with their corresponding indices, allowing direct computations with these elements and avoiding operations on zeros.

While such precomputation strategies are effective, they require significant memory to store the nonzero elements. In contrast, our approach avoids explicit storage of Hamiltonian elements and instead exploits the inherent sparsity of  $H$  to eliminate unnecessary computations. Here, we first analyze the structure of Hamiltonian matrix elements in SCI, which provides the foundation for our efficient computation strategy.

Suppose the Hamiltonian matrix element we need to compute is  $\langle D_{(w,u)} | H | D_{(x,v)} \rangle$ , which can be expressed as  $\langle S_w^\alpha | \langle S_u^\beta | H | S_x^\alpha \rangle | S_v^\beta \rangle$ . According to the Slater-Condon rules, this matrix element can be nonzero only if:

$$\text{DIFF}(S_w^\alpha, S_x^\alpha) + \text{DIFF}(S_u^\beta, S_v^\beta) \leq 2, \quad (4)$$

where  $\text{DIFF}(S_w, S_x)$  denotes the number of electron differences between bitstrings  $S_w$  and  $S_x$ . To classify these terms concisely, we introduce the notation  $[a, b]$ , where  $a = \text{DIFF}(S_w^\alpha, S_x^\alpha)$  and  $b = \text{DIFF}(S_u^\beta, S_v^\beta)$ . For example, the term  $[1, 1]$  corresponds to  $\text{DIFF}(S_w^\alpha, S_x^\alpha) = 1$  and  $\text{DIFF}(S_u^\beta, S_v^\beta) = 1$ . Throughout this work, we use the shorthand notations  $[2, 0]$ ,  $[1, 1]$ ,  $[1, 0]$ ,  $[0, 2]$ ,  $[0, 1]$ , and  $[0, 0]$  to represent a total of six terms in which the matrix elements may be nonzero. The first five terms correspond to off-diagonal elements of the Hamiltonian matrix, which are always computed on-the-fly. The last term,  $[0, 0]$ , corresponds to diagonal elements, which, although also computable on-the-fly, are precomputed and stored in memory in our program to improve efficiency.

Our novel algorithm for TBSCI is shown in Algorithm 1. Each Davidson iteration consists of  $N$  steps. In step  $q$ , the local process  $p$  performs the computation using data fetched from process  $q$ , which is detailed in Algorithm 1.

To eliminate unnecessary computations, we introduce the `SINGLE_LINK` and `DOUBLE_LINK` arrays, which store precomputed single and double excitation connections among  $\{S_u^\beta \mid u = 1, 2, \dots, l_\beta\}$ . These arrays ensure that Hamiltonian evaluations only occur when the electron difference between  $|D_{(w,u)}\rangle$  and  $|D_{(x,v)}\rangle$  does not exceed 2, directly eliminating invalid cases and improving efficiency. This optimization is particularly effective due to the unique structure of TBSCI: for each  $\alpha$  bitstring, the associated  $\beta$  bitstring set remains unchanged across determinants, allowing excitation connections to be precomputed and reused efficiently. In practice, these connections are stored as one-dimensional arrays to minimize memory usage, accompanied by auxiliary index arrays that record the starting positions and lengths of each column. For ease of explanation, however, we describe them as two-dimensional arrays throughout this paper.

As the `DOUBLE_LINK` array can be extremely large due to storing all double excitation connections between all  $\beta$  bitstrings, it is divided into batches, one per process, each containing a subset of  $\{S_u^\beta \mid u = 1, 2, \dots, l_\beta\}$ . For each  $S_u^\beta$ , the corresponding column `DOUBLE_LINK(:, S_u^\beta)` is constructed and stored entirely on a single process, and an auxiliary array records the

---

**Algorithm 1:** Conceptual algorithm for TBSCI on local process  $p$  at step  $q$ . This algorithm describes how to compute  $\langle S_w^\alpha | \langle S_u^\beta | H | S_x^\alpha \rangle | S_v^\beta \rangle$ , where  $\langle S_w^\alpha | \langle S_u^\beta |$  and  $| S_x^\alpha \rangle | S_v^\beta \rangle$  are determinants from processes  $p$  and  $q$ , respectively. For clarity, we present the algorithm without the symmetry optimization (Sec. 2.4.2) and reassignment strategy (Sec. 2.4.6).

---

**Data:**  $p$  the current process,  $q$  the current step.  
 SINGLE\_LINK and DOUBLE\_LINK lists.

```

1 for  $S_w^\alpha \leftarrow S_{p,1}^\alpha$  to  $S_{p,m_p}^\alpha$  do
2   for  $S_x^\alpha \leftarrow S_{q,1}^\alpha$  to  $S_{q,m_q}^\alpha$  do
3     case  $\leftarrow$  DIFP( $S_w^\alpha, S_x^\alpha$ )
4     if case = 2 then
5       for  $S_u^\beta \leftarrow S_1^\beta$  to  $S_{l_\beta}^\beta$  do
6          $S_v^\beta \leftarrow S_u^\beta$ 
7         Calculate [2,0] term
8       end for
9     else if case=1 then
10      for  $S_u^\beta \leftarrow S_1^\beta$  to  $S_{l_\beta}^\beta$  do
11        foreach  $S_v^\beta \in$  SINGLE_LINK( $:, S_u^\beta$ ) do
12          Calculate [1,1] term
13        end foreach
14         $S_v^\beta \leftarrow S_u^\beta$ 
15        Calculate [1,0] term
16      end for
17    else if case=0 then
18      for  $S_u^\beta \leftarrow S_1^\beta$  to  $S_{l_\beta}^\beta$  do
19        foreach  $S_v^\beta \in$  SINGLE_LINK( $:, S_u^\beta$ ) do
20          Calculate [0,1] term
21        end foreach
22         $S_v^\beta \leftarrow S_u^\beta$ 
23        Calculate [0,0] term
24      end for
25    end if
26  end for
27   $S_x^\alpha \leftarrow S_w^\alpha$ 
28  foreach  $S_u^\beta \in$  the  $q$ -th batch of  $\{S^\beta\}$  do
29    foreach  $S_v^\beta \in$  DOUBLE_LINK( $:, S_u^\beta$ ) do
30      Calculate [0,2] term
31    end foreach
32  end foreach
33 end for

```

---

index range assigned to each process to facilitate data access. Consequently, the computation of the  $[0,2]$  term is carried out batch by batch over the  $N$  steps (Lines 27–32 of Algorithm 1). Since this term involves only a loop over  $S_w^\alpha$ , without referencing  $S_x^\alpha$ , each process  $p$  needs to fetch `DOUBLE_LINK` data from the target process  $q$  only once per Davidson step.

In contrast, the `SINGLE_LINK` array has to be replicated on each node; otherwise, MPI communication would be too frequent, as it is accessed over both  $S_w^\alpha$  and  $S_x^\alpha$  (Line 11 of Algorithm 1). It is reasonable to assume that the sparsities of single and double excitations scales as  $\sqrt{N_{\text{SCI}}/N_{\text{FCI}}}$ . Thus, the storage requirement of `SINGLE_LINK` is approximately  $l_\beta \cdot N_{\text{occ}} \cdot N_{\text{vir}} \cdot \sqrt{N_{\text{SCI}}/N_{\text{FCI}}}$ , where  $N_{\text{occ}}$  and  $N_{\text{vir}}$  denote the numbers of occupied and virtual orbitals, respectively. This may become a memory bottleneck when  $l_\beta$  becomes large; in such a case, single excitations may be generated on-the-fly, at the cost of additional computation. However, since the limitation did not arise in the present study and may not occur in future applications—given that  $\sqrt{N_{\text{SCI}}/N_{\text{FCI}}}$  can be very small—we do not pursue its resolution here.

As shown in Algorithm 1, this sparsity factor ( $\sqrt{N_{\text{SCI}}/N_{\text{FCI}}}$ ) appears once in the computations of the  $[2,0]$  and  $[0,2]$  terms, but twice in that of the  $[1,1]$  term. Consequently, the dominant contributions come from the  $[2,0]$  and  $[0,2]$  terms, each scaling as  $N_{\text{SCI}} \cdot N_{\text{occ}}^2 \cdot N_{\text{vir}}^2 \cdot \sqrt{N_{\text{SCI}}/N_{\text{FCI}}}$ , while the  $[1,1]$  term has a smaller scaling of  $N_{\text{SCI}} \cdot N_{\text{occ}}^2 \cdot N_{\text{vir}}^2 \cdot N_{\text{SCI}}/N_{\text{FCI}}$ . In practice, the  $[0,2]$  term is the most time-consuming, as the information for double excitations between  $S_w^\beta$  and  $S_u^\beta$  is evaluated within the innermost loop. As mentioned earlier, our TBSCI program can also be used to perform FCI calculations. In this case, the sparsity factor becomes exactly one, and the computational cost simplifies to  $N_{\text{FCI}} \cdot N_{\text{occ}}^2 \cdot N_{\text{vir}}^2$ , with the dominant contributions arising from the  $[2,0]$ ,  $[1,1]$ , and  $[0,2]$  terms. In practice, when our implementation is used for FCI the  $[1,1]$  term is the most time-consuming. It should be emphasized that the computational cost of the Handy–Knowles FCI algorithm scales only as  $N_{\text{FCI}} \cdot N_{\text{occ}} \cdot N_{\text{vir}}$ ; as such, our intention is not to compete with existing FCI methods, but rather to showcase both the algorithmic effectiveness of the newly designed TBSCI method

and the high efficiency enabled by our parallelization strategies. A summary of the scaling behavior and the dominant terms is provided in Table 1.

Table 1: Computational scaling and dominant terms of SCI and FCI calculations in the framework of TBSCI.

Method	Overall scaling	Dominant terms
SCI	$N_{\text{SCI}} \cdot N_{\text{occ}}^2 \cdot N_{\text{vir}}^2 \cdot \sqrt{N_{\text{SCI}}/N_{\text{FCI}}}$	[2, 0], [0, 2]
FCI	$N_{\text{FCI}} \cdot N_{\text{occ}}^2 \cdot N_{\text{vir}}^2$	[2, 0], [1, 1], [0, 2]

## 2.4 Strategies for Efficient Parallel Execution in TBSCI

As described above, we distribute the CI vector across nodes to overcome single-node memory limitations, enabling computations to fully utilize the total available memory. However, this distributed storage introduces new challenges: a computation that could previously be completed in a single step now requires  $N$  steps, with each step requiring data retrieval from a target process [as shown in Eq. (3)]. As the number of nodes increases, the overall MPI communication volume seemingly scales as  $N_{\text{SCI}}^2$ , making communication latency a potential bottleneck for computational efficiency. To address this issue, we have developed a suite of strategies to reduce communication overhead and improve parallel execution.

### 2.4.1 Avoiding Unnecessary MPI Data Transfers

In our previous analysis, we mentioned that each local process  $p$  needs to fetch data from other processes. However, not all data from the target process is required. Specifically, if all  $\alpha$  bitstrings assigned to process  $p$ , namely  $\{S_{p,1}^\alpha, S_{p,2}^\alpha, \dots, S_{p,m_p}^\alpha\}$ , satisfy  $\text{DIFF}(S_w^\alpha, S_x^\alpha) > 2$  for any  $S_w^\alpha$  in this set, then process  $p$  does not need the segment corresponding to  $S_x^\alpha$ .

In our implementation, such information is precomputed and stored, allowing each process to identify and skip unnecessary data transfers, thereby significantly improving communication efficiency. As a result, the MPI communication volume for process  $p$  roughly scales as  $m_p \cdot N_{\text{occ}}^2 \cdot N_{\text{vir}}^2 \cdot \sqrt{N_{\text{SCI}}/N_{\text{FCI}}} \cdot l_\beta$ , matching the scaling of the local computational

cost. Consequently, the total MPI communication volume across all nodes scales as  $N_{\text{SCI}}$ , rather than  $N_{\text{SCI}}^2$ , providing a solid foundation for the efficient parallel execution of TBSCI in large-scale calculations involving many nodes on supercomputers.

### 2.4.2 Exploiting Molecular Symmetry

Exploiting molecular symmetry is a well-established practice in quantum chemistry to enhance computational efficiency. Building upon the strategy of avoiding unnecessary MPI data transfers, leveraging molecular symmetry can further reduce the data transfer volume in the TBSCI framework. As shown in Algorithm 1, the segments satisfying  $\text{DIFF}(S_w^\alpha, S_x^\alpha) = 2$ , which are typically much more than those satisfying  $\text{DIFF} = 1$ , are used solely for computing the  $[2, 0]$  term. In this case, because the  $\beta$  bitstrings must match exactly ( $S_v^\beta \equiv S_u^\beta$ ),  $S_w^\alpha$  and  $S_x^\alpha$  must belong to the same symmetry sector, otherwise the corresponding Hamiltonian matrix element vanishes. Thus, molecular symmetry naturally restricts the possible communication targets and further reduces MPI communication. This strategy becomes particularly effective for molecules with high symmetry. For example, in systems with  $D_{2h}$  symmetry, memory usage drops by  $\sim 8\times$ , and computational cost and data transfer volume drop by  $\sim 64\times$ .

However, in this case, the selected determinants are no longer constructed as tensor products of independently selected  $\alpha$  and  $\beta$  bitstrings, but are further restricted—on top of the original tensor-product construction—to those consistent with the target symmetry. As a result, the storage layout no longer strictly follows the structure shown in Figure 1, and the computation is no longer performed strictly according to Algorithm 1, as only symmetry-allowed combinations are evaluated. Nevertheless, for clarity, we retain the original forms of both Figure 1 and Algorithm 1.

### 2.4.3 Minimizing Long-Distance Communication in MPI

Each node in the supercomputer is assigned a unique node identity number (ID) ranging from 0 to  $N - 1$ . When nodes are appropriately ordered, messages sent between nodes with closer IDs tend to require fewer network hops than those between nodes with larger ID differences.

Leveraging this property, we sort the selected  $\alpha$  bitstrings according to their excitation levels relative to the Hartree–Fock (HF)  $\alpha$  bitstring, and assign them to nodes in increasing order. Hence, lower-excitation  $\alpha$  bitstrings are allocated to lower-numbered nodes, while higher-excitation bitstrings are assigned to higher-numbered nodes.

This excitation-aware mapping can significantly reduce MPI communication between distant nodes. Since the excitation differences between the  $\alpha$  bitstrings assigned to distant nodes are more likely to exceed two, remote data retrieval is usually unnecessary. As a result, and quite remarkably, even in massively parallel jobs involving thousands or tens of thousands of nodes, each node primarily fetches data from its neighboring nodes. This locality-preserving strategy plays a critical role in alleviating MPI communication congestion and enables our SCI program to maintain high parallel efficiency even on computations involving thousands or tens of thousands of nodes.

### 2.4.4 Achieving Memory and Computational Load Balance in MPI

As shown in Algorithm 1, the computational cost associated with each segment corresponding to a given  $S_w^\alpha$  can be readily estimated. Consequently, the total workload of a process can be approximated by summing the estimated costs of all  $\alpha$  bitstrings assigned to it. As described above, we assign  $\alpha$  bitstrings to processes in increasing order of their excitation levels relative to the HF  $\alpha$  bitstring, a strategy that is crucial in our parallel execution. Based on this excitation-aware mapping, achieving simultaneous balance in memory usage and computational workload becomes a nontrivial problem.

Since the total number of  $\alpha$  bitstrings is fixed, the average number per process is predeter-

mined. Likewise, the total estimated cost is fixed, implying that the average computational load per process is also predetermined. Therefore, we can define two expansion factors to quantify the tradeoff between memory and computation: the *memory expansion factor*, defined as the ratio of the assigned  $\alpha$  bitstring count to the average, and the *computation expansion factor*, defined as the ratio of the estimated computational cost to the average. Enforcing strict memory balance (i.e., keeping the memory expansion factor close to 1) can result in severe computational imbalance, causing some processes to complete significantly earlier and remain idle while others continue. Conversely, enforcing strict computational balance (i.e., keeping the computation expansion factor close to 1) may lead to a highly uneven memory usage, with some nodes exceeding their memory limits, thereby forcing an increase in the total number of nodes and leading to inefficient resource usage.

To address this issue, we adopt a balanced strategy where both expansion factors are maintained to be moderately greater than 1, ensuring that neither memory imbalance nor computational imbalance becomes excessive. In the special case of FCI calculations—used here solely for testing purposes—the computational cost per segment is exactly the same, and thus a simple uniform distribution strategy naturally ensures both memory and workload balance.

#### 2.4.5 Overlapping Computation and Data Transfer

As mentioned above, each node in our program runs a single process. Modern computers are typically multi-core; for example, each node on supercomputer Fugaku has 48 CPU cores. Even though we minimize unnecessary data transfers and reduce long-distance communication, some degree of MPI communication congestion remains unavoidable. The question then arises: how can we further mitigate its impact on the overall computation wall time?

To mitigate this issue, one core is assigned to perform MPI data transfers, fetching the required data for the next step, while the remaining 47 cores perform parallel computation for the current step using OpenMP. Let  $t_{\text{cal}}$  and  $t_{\text{data}}$  represent the computation time and

the data retrieval time of one step, respectively. If  $t_{\text{data}} > t_{\text{cal}}$ , we define the delay time to the wall time as  $t_{\text{delay}} = t_{\text{data}} - t_{\text{cal}}$ . Conversely, if  $t_{\text{data}} \leq t_{\text{cal}}$ , then  $t_{\text{delay}} = 0$ , since MPI communication congestion during data transfer—if it occurs—does not prolong the wall time. The total delay time  $T_{\text{delay}}$  for a Davidson iteration is defined as the sum of  $t_{\text{delay}}$  over all  $N$  steps of a process. As the wall time is determined by the slowest process, we only report the  $T_{\text{delay}}$  observed on that process in the Section 3. As the single-precision implementation involves only half the data volume of the double-precision case, its  $T_{\text{delay}}$  is expected to be significantly smaller, as confirmed by our numerical experiments.

#### 2.4.6 Reassignment of $[0, 2]$ for Delay Absorption

Since data retrieval and computation are executed concurrently, delays ( $t_{\text{delay}} > 0$ ) are more likely to occur in steps where the computational time  $t_{\text{cal}}$  is relatively small. Through careful analysis, we observe that the  $[0, 2]$  term (Lines 27–32 in Algorithm 1) exhibits a favorable computational pattern: while being one of the dominant terms in both SCI and FCI calculations, it incurs substantial computational cost but only negligible data retrieval.

We therefore treat the  $[0, 2]$  tasks as a computational reservoir to absorb potential delays. Each process reassigns its  $N$  batches of  $[0, 2]$  tasks to steps where  $t_{\text{cal}}$  is pre-estimated to be small, thereby reducing both the probability and magnitude of  $t_{\text{delay}}$ . As discussed in Section 2.4.3, a local process may not need to retrieve any data from certain target processes due to the excitation-aware mapping. In such cases, delays are unlikely to occur, and the corresponding  $[0, 2]$  task for those steps are reassigned to other steps with small  $t_{\text{cal}}$ .

Due to this reassignment performed prior to execution, the actual execution no longer strictly follows the “one step computes one batch of `DOUBLE_LINK`” structure outlined in Algorithm 1. Instead, some steps may process multiple batches of  $[0, 2]$  tasks, some may process none, and some may be entirely skipped by process  $p$ . Nevertheless, for clarity, we still retain the original form of Algorithm 1.

### 2.4.7 Odd-Even Process Fetch Strategy

A large number of simultaneous MPI data transfers can lead to communication peaks in the network. To alleviate this issue, we introduce an odd–even process fetch strategy. For each process, the target ranks are sorted by the number of required segments. Odd-numbered processes fetch data in ascending order, while even-numbered processes fetch in descending order. This simple strategy effectively reduces both the frequency and magnitude of  $T_{\text{delay}}$ , particularly in simulations involving thousands or tens of thousands of nodes.

### 2.4.8 “Check if Busy” Strategy for Communication

During data fetching from target processes, we employ a strategy called “Check if Busy”. Specifically, when process A uses `MPI_GET` to fetch data from process B, both A and B are marked as `BUSY`. During this period, no other process can fetch data from either A or B; instead, they will first fetch data from processes that are `NOT BUSY`. This strategy helps prevent multiple processes from simultaneously accessing the same process, thereby reducing communication congestion and improving overall parallel efficiency.

### 2.4.9 Sleep Strategy under Severe MPI Congestion

Even with the above MPI optimization strategies, we still sometimes observe unexpectedly large values of  $T_{\text{delay}}$  when using more than 5,000 nodes. Surprisingly, for the same system and input settings,  $T_{\text{delay}}$  can be nearly zero in one run, but over 100 seconds in another. This instability is partly caused by external factors, such as MPI traffic from other jobs running at the same time, or different node placements by the job scheduler. However, we believe the deeper reason lies in the nature of MPI congestion. It is like a traffic jam: once congestion occurs, it induces blocking behavior, which in turn worsens further congestion. This kind of chain reaction becomes harder to control when using more nodes.

To address this, we design a sleep strategy. Once a process finds that  $t_{\text{delay}} > 0.2$  seconds for a given step, it is interpreted as an indication of severe congestion. The process then

sleeps for 0.1 seconds to mitigate further blocking. While sleeping, the process is marked as `BUSY`, so that other processes will preferentially fetch data from other sources. Naturally, the sleep time is included in the measured  $T_{\text{delay}}$ .

Unlike the previous strategies, this sleep strategy may slightly increase the total  $T_{\text{delay}}$  of a single Davidson iteration. However, in all of our tests, it consistently eliminates large delay events, making it a practical and effective safeguard. The specific thresholds of 0.2 and 0.1 seconds are chosen empirically based on our experience on Fugaku; different systems and applications may require fine-tuning of these parameters.

### 3 Results

We first generated the HF reference states and corresponding FCIDUMP files using PySCF.<sup>22</sup> Subsequently, TBSCI calculations were performed on the supercomputer Fugaku. The convergence criterion was defined as an energy difference of less than  $2 \times 10^{-7}$  Hartree between consecutive iterations. It should be noted that all the FCI data presented in this work were recomputed using our TBSCI program, although some of the results have been previously reported.<sup>23,24</sup> Fugaku features a CPU-only architecture based on the A64FX processor. Each node contains 48 cores and only 32 GiB of memory, making both computational and memory distribution essential for large-scale execution. The TBSCI code was compiled using the Fujitsu compiler with the `-Kfast,parallel,openmp,SVE` flags. To demonstrate the performance of our code, we report the time of a single distributed matrix-vector multiplication ( $\mathbf{W} = \mathbf{H} \cdot \mathbf{U}$ ) for different numbers of processes; the wall time of this multiplication is almost as same as that of one Davidson iteration. Throughout all calculations, all data, including the CI vector and intermediate arrays, were kept entirely in memory without disk I/O, ensuring minimal data access latency.

### 3.1 N<sub>2</sub> with the aug-cc-pVDZ Basis Set

We first test the performance of TBSCI by computing the potential energy surface (PES) of N<sub>2</sub> using the aug-cc-pVDZ basis set. Under D<sub>2h</sub> symmetry and the frozen-core approximation, each geometry point yields  $1.47 \times 10^{11}$  determinants.

Table 2: Potential energy surface of N<sub>2</sub> computed with the aug-cc-pVDZ basis set at various bond lengths ( $R$ ). HF and FP64 (double-precision) FCI energies are reported in Hartree ( $E_h$ ), and FP32 (single-precision) deviations from FP64 are shown in units of  $10^{-6} E_h$ .

$R$ (Bohr)	HF	FP64	FP32
2.068	-108.961045	-109.295263	1
2.4	-108.875323	-109.258928	1
2.7	-108.748038	-109.182160	0
3.0	-108.618929	-109.108790	0
3.6	-108.401280	-109.016333	-3
4.2	-108.242916	-109.986039	-9

To validate the numerical accuracy of the single-precision implementation, we compute the FCI energies at several bond lengths using both precision variants. As shown in Table 2, the results are nearly identical across all bond lengths, with the largest deviation observed at  $R = 4.2$  Bohr, where the difference is only  $0.009 mE_h$ . While these differences remain well below chemical accuracy, we note that the discrepancy tends to increase at stretched geometries, where convergence requires more Davidson iterations (up to 49 iterations at  $R = 4.2$  Bohr). This suggests that although single precision is generally sufficient for SCI calculations, additional care may be needed when many iterations are required.

The MPI performance of both precision variants is summarized in Table 3. We begin by analyzing the MPI communication delay, characterized by the total  $T_{\text{delay}}$  on the slowest process. Both precision variants show satisfactory performance in this regard. Remarkably,  $T_{\text{delay}}$  is exactly zero in all single-precision runs, highlighting the benefit of reduced data volume in mitigating MPI congestion. Next, we assess MPI load balancing using the ratio of maximum to average wall time. Across all node counts, this ratio remains within 105%, confirming that the uniform distribution of  $\alpha$  bitstrings achieves both memory and computa-

Table 3: Parallel performance of TBSCI for  $N_2$  computed with the aug-cc-pVDZ basis set using both double- and single-precision (FP64 and FP32) implementations. For each case, we report the average wall time (Avg.), maximum wall time (Max.), and delay time ( $T_{\text{delay}}$ , see Sec. 2.4.5) of a single distributed matrix-vector multiplication in seconds, as well as the total node hours (NHs) consumed.

Nodes	FP64				FP32			
	Avg.	Max.	$T_{\text{delay}}$	NHs	Avg.	Max.	$T_{\text{delay}}$	NHs
480	2030	2088	0	278	1942	1997	0	266
960	1016	1053	0.1	281	968	1007	0	269
1440	676	704	0.3	282	645	673	0	269
1920	509	531	10.4	283	484	505	0	269
2400	407	426	4.2	284	387	405	0	270
2880	341	358	0.7	286	325	340	0	272

tional balance in FCI calculations. Finally, we evaluate strong scaling efficiency by tracking the total node hours (NHs) with increasing node counts. As shown in Table 3, NHs increase only slightly, indicating that the implementation maintains near-ideal strong scaling up to almost 3,000 nodes.

### 3.2 CN with the cc-pVTZ Basis Set

The next tested system is an open-shell molecule, CN. Under  $C_{2v}$  symmetry with frozen core orbitals, the number of determinants reaches  $2.46 \times 10^8$  and  $4.86 \times 10^{11}$  under the cc-pVDZ and cc-pVTZ basis sets, respectively.

In Table 4, FCI energies are computed along the PES up to a bond length of  $2.3 \text{ \AA}$  using both basis sets. The largest deviation between the two basis sets occurs at  $R = 2.3 \text{ \AA}$ , where the difference is only  $0.004 mE_h$ . In addition, as our calculations represent one of only a few systems that can be computed with a triple- $\zeta$  quality basis set by FCI, we also perform 2/3 extrapolation of the FP64 energies to the complete basis set limit (CBS). We extrapolate the HF energy ( $E_c^{\text{HF}}$ ) of a given cardinality ( $c$ ) as  $\text{CBS}(l/m) = E_m^{\text{HF}} - \frac{(E_m^{\text{HF}} - E_l^{\text{HF}})m^{-5}}{m^{-5} - l^{-5}}$  and the correlation energy ( $E_c^{\text{Cor}}$ ) as  $\text{CBS}(l/m) = E_m^{\text{Cor}} - \frac{(E_m^{\text{Cor}} - E_l^{\text{Cor}})m^{-3}}{m^{-3} - l^{-3}}$ .<sup>25</sup> The results in Table 4 can be served as valuable benchmarks for future research in quantum chemistry.

Table 4: Potential energy surfaces of CN computed with the cc-pVDZ and cc-pVTZ basis sets. HF and FP64 FCI energies are reported in Hartree ( $E_h$ ), and FP32 deviations from FP64 are shown in units of  $10^{-6} E_h$ . The FP64 energies are extrapolated to the complete basis set (CBS) limit using a two-point formula, denoted as CBS( $l/m$ ), where  $l$  and  $m$  denote the cardinalities of the basis sets.

$R$ (Å)	cc-pVDZ			cc-pVTZ			CBS(2/3)
	HF	FP64	FP32	HF	FP64	FP32	FP64
1.16	-92.197616	-92.491811	0	-92.219490	-92.569252	0	-92.595966
1.3	-92.149983	-92.479361	0	-92.168341	-92.550251	1	-92.575154
1.5	-92.041711	-92.408658	1	-92.059594	-92.476056	1	-92.499617
1.7	-91.937733	-92.334641	0	-91.957354	-92.400739	-1	-92.423284
2.0	-91.822293	-92.262054	-1	-91.844595	-92.324826	-1	-92.345249
2.3	-91.704156	-92.242169	4	-91.727232	-92.300497	-1	-92.318840

Table 5: Parallel performance of TBSCI for CN computed with the cc-pVTZ basis set using both FP64 and FP32 implementations. For each case, we report the average wall time (Avg.), maximum wall time (Max.), and delay time ( $T_{\text{delay}}$ ) of a single distributed matrix-vector multiplication in seconds, as well as the total node hours (NHs) consumed.

Nodes	FP64				FP32			
	Avg.	Max.	$T_{\text{delay}}$	NHs	Avg.	Max.	$T_{\text{delay}}$	NHs
1600	5516	5743	0	2552	5026	5265	0	2340
2400	3655	3809	0	2539	3331	3478	0	2319
4800	1824	1909	0.5	2545	1650	1743	0	2324
7200	1227	1315	18.1	2630	1110	1224	0	2448
9600	938	1070	8.3	2853	839	1003	0	2675

The MPI performance of TBSCI for CN with the cc-pVTZ basis set is summarized in Table 5. While the double-precision variant shows modest delays at high node counts (e.g., 18.1 seconds at 7200 nodes), the single-precision variant consistently shows zero delay on the slowest process in all tests—even at 9,600 nodes. Such excellent performance once again highlights the advantage of reduced data volume in large-scale high-performance computing (HPC) environments. At 9600 nodes, the ratio of maximum to average wall time increases to nearly 120%, indicating growing MPI load imbalance. Although in FCI calculations each segment should, in principle, have the same computational cost, such balance cannot be

maintained once the workload is divided into multiple steps. Because perfect parallelism cannot be achieved within each step, increasing the number of steps—an inevitable consequence of using more nodes—leads to wall-time differences between processes. As a result, MPI load imbalance becomes more significant at larger node counts, leading to the observed increase in NHs. Nevertheless, from 1600 to 9600 nodes, the total NHs increase by only 14%, highlighting the exceptional performance enabled by the MPI optimization strategies we have designed.

### 3.3 Cr<sub>2</sub> with the STO-3G Basis Set

Cr<sub>2</sub> is a challenging molecule in quantum chemistry, exhibiting strong static and dynamic correlation even near its equilibrium geometry. With the minimal STO-3G basis set, the FCI dimension still reaches  $9.14 \times 10^{11}$  under D<sub>2h</sub> symmetry with 12 core orbitals frozen.

Table 6: Energies of Cr<sub>2</sub> computed with various methods using the STO-3G basis set at  $R = 1.5 \text{ \AA}$ .

Methods	Energy
HF	-2064.078900
CCSD(T)	-2064.781602
CCSDT	-2064.780060
CCSDTQ	-2064.802602
FP64	-2064.808195
FP32	-2064.808195

Various orders of coupled cluster (CC) methods, including CCSD(T), CCSDT,<sup>26–28</sup> and CCSDTQ,<sup>29,30</sup> were computed using NWChem.<sup>31</sup> As shown in Table 6, the FCI energies (FP64 and FP32) are approximately 5.6 mE<sub>h</sub> lower than the CCSDTQ result, highlighting the difficulty of accurately calculating this transition metal diatomic molecule.

For large-scale systems, we recommend using the single-precision implementation, as it provides sufficient numerical accuracy while significantly improving MPI efficiency compared to the double-precision variant. Therefore, all subsequent tests focus exclusively on the

Table 7: Parallel performance of TBSCI for  $\text{Cr}_2$  computed with the STO-3G basis set using the single-precision implementation. We report the average wall time (Avg.), maximum wall time (Max.), and delay time ( $T_{\text{delay}}$ , see Sec. 2.4.5) of a single distributed matrix-vector multiplication in seconds, as well as the total node hours (NHs) consumed.

Nodes	Avg.	Max.	$T_{\text{delay}}$	NHs
2880	1098	1119	0.4	895
5760	551	567	2.2	907
8640	373	383	7.4	919
11520	281	293	8.1	938
14400	227	242	17.3	968

single-precision variant. As summarized in Table 7,  $T_{\text{delay}}$  remains below 18 seconds even when using more than 14,000 nodes. The ratio of maximum to average wall time remains within 107%, and the total NHs increase by less than 9% from 2,880 to 14,400 nodes. These results demonstrate not only near-ideal parallel efficiency but also excellent scalability: even as both the system size and node count grow substantially, our implementation consistently maintains exceptional performance. This underscores the strength and robustness of our MPI optimization strategies in handling large-scale computations.

### 3.4 $\text{N}_2$ with the cc-pVTZ Basis Set

The final system is  $\text{N}_2$  with the cc-pVTZ basis set at  $R = 2.068$  Bohr. This calculation involves  $2.62 \times 10^{12}$  determinants under  $D_{2h}$  symmetry with core orbitals frozen, which is approximately twice the size of the largest reported FCI calculation to date ( $1.31 \times 10^{12}$  determinants).

Table 8: HF and FCI energies (single-precision) of  $\text{N}_2$  at  $R = 2.068$  Bohr computed with the cc-pVDZ and cc-pVTZ basis sets. The FCI energies are extrapolated to the complete basis set (CBS) limit using a two-point formula.

cc-pVDZ			cc-pVTZ			CBS(2/3)
HF	FP32		HF	FP32		FP32
-108.954553	-109.276527		-108.984093	-109.375153		-109.408722

For this large system, we only run with the single-precision variant, as shown in Table 8. The resulting FCI energies for  $N_2$  at the cc-pVTZ and CBS levels provide important new benchmark data for future studies in quantum chemistry. It is worth noting that Alavi *et al.* previously tested the same system using their FCIQMC method in 2010, reporting an energy of  $-109.37491 E_h$ .<sup>32</sup> The error of this calculation with respect to the exact FCI energy is only 0.24  $mE_h$ , demonstrating the impressive accuracy achieved by their stochastic method more than 15 years ago.

Table 9: Parallel performance of TBSCI for  $N_2$  computed with the cc-pVTZ basis set using single-precision implementations. We report the average wall time (Avg.), maximum wall time (Max.), and delay time ( $T_{\text{delay}}$ ) of a single distributed matrix-vector multiplication in seconds, as well as the total node hours (NHs) consumed.

Nodes	Avg.	Max.	$T_{\text{delay}}$	NHs
12000	2582	2924	0.9	9747
18000	1726	2076	0.3	10380
24000	1346	1630	2.4	10876
30000	1102	1413	12.8	11775
36000	917	1201	8.2	12010

As summarized in Table 9,  $T_{\text{delay}}$  remains below 13 seconds even with more than 30,000 nodes, demonstrating the remarkable communication efficiency achieved by our MPI optimization strategies. However, as the number of nodes increases, the ratio of maximum to average wall time becomes significantly larger, reaching 131% at 36,000 nodes. Meanwhile, the total NHs increase about 23% from 12,000 to 36,000 nodes. Considering the use of tens of thousands of nodes, such load imbalance is acceptable, and the overall parallel performance remains excellent. Further improvements to the TBSCI program are planned for future work.

## 4 Conclusions and Prospects

In this work, we have proposed and implemented a completely new and highly efficient algorithm for the tensor-product bitstring SCI (TBSCI), in which the selected determinants

are constructed as tensor products of important bitstrings.<sup>17</sup> To overcome the memory limitations of a single node, we have, for the first time worldwide, implemented distributed storage of the CI vector in the TBSCI program, allowing the entire memory resources of a supercomputer to be utilized for large-scale computations.

To reduce MPI communication congestion, we developed a suite of strategies including avoiding unnecessary communication, leveraging molecular symmetry, reducing long-distance data transfers, balancing computational load and memory usage, overlapping communication and computation through prefetching, reassigning fast-fetch [0, 2] tasks, implementing staggered fetch strategies, detecting process status prior to data access, and applying a sleep strategy. These innovations were not developed all at once, but were progressively identified and validated through several months of intensive testing, profiling, and iteration. As these strategies were integrated, the communication delay of the slowest process ( $T_{\text{delay}}$ ) was drastically reduced. The parallel capabilities of TBSCI enabled an SCI-based calculation of  $\text{N}_2$  using the cc-pVTZ basis set with  $2.62 \times 10^{12}$  determinants—more than three orders of magnitude beyond the previous SCI record ( $2 \times 10^9$  determinants)<sup>12</sup> and about twice the scale of the largest reported FCI calculation ( $1.31 \times 10^{12}$  determinants).<sup>5</sup> Despite this scale, the TBSCI single-precision implementation exhibited no communication delay under 10,000 nodes, and maintained an exceptional performance with under 18 seconds delay even at 36,000 nodes, marking a new level of MPI efficiency in large-scale SCI.

Looking forward, a critical next step is the incorporation of second-order perturbative corrections atop the distributed SCI framework. Because TBSCI is the first SCI implementation with distributed CI vector storage, corresponding perturbative corrections must also be implemented in a distributed manner, requiring new algorithms and implementations. This presents substantial technical challenges which will be the subject of future work.

Additionally, we are exploring the development of a fully classical bitstring selection strategy, which would enable TBSCI to operate entirely on classical hardware. Such a version may even outperform hybrid quantum-classical approaches by avoiding the detrimental

effects of quantum noise and enabling complete reproducibility.

Finally, the distributed storage scheme and MPI communication optimization strategies developed in this work are not limited to TBSCI. Rather, they constitute a general and scalable framework for large-scale CI implementations, and can be readily adapted to various SCI variants, as well as semistochastic CI methods.<sup>33,34</sup>

We believe this work lays the foundation for a new generation of parallel electronic structure methods capable of addressing strongly correlated systems at unprecedented scale. It also marks a new stage for SCI, driven by distributed CI vector storage and communication optimization strategies.

## Acknowledgments

The authors thank Muneaki Kamiya for suggesting a subspace restart strategy in the Davidson algorithm to reduce memory usage, and Himadri Pathak for discussions on applications

## References

- (1) Knowles, P. J.; Handy, N. C. A new determinant-based full configuration interaction method. *Chem. Phys. Lett.* **1984**, *111*, 315–321.
- (2) Ansaloni, R.; Bendazzoli, G. L.; Evangelisti, S.; Rossi, E. A parallel Full-CI algorithm. *Comput. Phys. Commun.* **2000**, *128*, 496–515.
- (3) Gan, Z.; Alexeev, Y.; Gordon, M. S.; Kendall, R. A. The parallel implementation of a full configuration interaction program. *J. Chem. Phys.* **2003**, *119*, 47–59.
- (4) Fales, B. S.; Levine, B. G. Nanoscale Multireference Quantum Chemistry: Full Configuration Interaction on Graphical Processing Units. *J. Chem. Theory Comput.* **2015**, *11*, 4708–4716.

- (5) Gao, H.; Imamura, S.; Kasagi, A.; Yoshida, E. Distributed implementation of full configuration interaction for one trillion determinants. *J. Chem. Theory Comput.* **2024**, *20*, 1185–1192.
- (6) Raghavachari, K.; Trucks, J. A.; Pople, J. A.; Head-Gordon, M. A fifth-order perturbation comparison of electron correlation theories. *Chem. Phys. Lett.* **1989**, *157*, 479.
- (7) Huron, B.; P., M. J.; R., R. Iterative perturbation calculations of ground and excited state energies from multiconfigurational zeroth-order wavefunctions. *J. Chem. Phys.* **1973**, *58*, 5745–5759.
- (8) Tubman, N. M.; Lee, J.; Takeshita, T. Y.; Head-Gordon, M.; Whaley, K. B. A deterministic alternative to the full configuration interaction quantum Monte Carlo method. *J. Chem. Phys.* **2016**, *145*, 044112.
- (9) Williams-Young, D. B.; Tubman, N. M.; Mejuto-Zaera, C.; de Jong, W. A. A parallel, distributed memory implementation of the adaptive sampling configuration interaction method. *J. Chem. Phys.* **2023**, *158*, 214109.
- (10) Holmes, A. A.; M., T. N.; Umrigar, C. J. Heat-Bath Configuration Interaction: An Efficient Selected Configuration Interaction Algorithm Inspired by Heat-Bath Sampling. *J. Chem. Theory Comput.* **2016**, *12*, 3674–3680.
- (11) Sharma, S.; Holmes, A. A.; Jeanmairet, G.; Alavi, A.; Umrigar, C. J. Semistochastic Heat-Bath Configuration Interaction Method: Selected Configuration Interaction with Semistochastic Perturbation Theory. *J. Chem. Theory Comput.* **2017**, *13*, 1595–1604.
- (12) Li, J.; Matthew., O.; Holmes, A. A.; Sharma, S.; Umrigar, C. J. Fast semistochastic heat-bath configuration interaction. *J. Chem. Phys.* **2018**, *149*, 214110.
- (13) Liu, W.; Hoffmann, M. R. iCI: Iterative CI toward full CI. *J. Chem. Theory Comput.* **2016**, *12*, 1169–1178.

- (14) Zhang, N.; Liu, W.; Hoffmann, M. R. Iterative Configuration Interaction with Selection. *J. Chem. Theory Comput.* **2020**, *16*, 2296–2316.
- (15) Zhang, N.; Liu, W.; Hoffmann, M. R. Further Development of iCIPT2 for Strongly Correlated Electrons. *J. Chem. Theory Comput.* **2021**, *17*, 949–964.
- (16) Keita, K.; Masaya, K.; Ryosuke, I.; Sho, K.; Kosuke, M.; Wataru, M.; Yuya, O. N. Quantum-Selected Configuration Interaction: classical diagonalization of Hamiltonians in subspaces selected by quantum computers. **2023**, arXiv:2302.11320.
- (17) Robledo-Moreno, J.; Motta, M.; Haas, H.; Javadi-Abhari, A.; Jurcevic, P.; Kirby, W.; Martiel, S.; Sharma, K.; Sharma, S.; Shirakawa, T.; Sitdikov, I.; Sun, R.-Y.; Sung, K. J.; Takita, M.; Tran, M. C.; Yunoki, S.; Mezzacapo, A. Chemistry Beyond Exact Solutions on a Quantum-Centric Supercomputer. **2024**, arXiv:2405.05068.
- (18) Pakiari, A. H.; Handy, N. C. The configuration interaction method, and the triplet-singlet splitting in CH<sub>2</sub>. *Theor. Chim. Acta* **1975**, *40*, 17–23.
- (19) Pokhilko, P.; Epifanovsky, E.; Krylov, A. I. Double Precision Is Not Needed for Many-Body Calculations: Emergent Conventional Wisdom. *J. Chem. Theory Comput.* **2018**, *14*, 4088–4096.
- (20) Davidson, E. R. The iterative calculation of a few of the lowest eigenvalues and corresponding eigenvectors of large real-symmetric matrices. *J. Comput. Phys.* **1975**, *17*, 87–94.
- (21) Garniron, Y.; Applencourt, T.; Gasperich, K.; Benali, A.; Ferté, A.; Paquier, J.; Pradines, B.; Assaraf, R.; Reinhardt, P.; Toulouse, J.; Barbaresco, P.; Renon, N.; David, G.; Malrieu, J.-P.; Vêril, M.; Caffarel, M.; Loos, P.-F.; Giner, E.; Scemama, A. Quantum Package 2.0: An Open-Source Determinant-Driven Suite of Programs. *J. Chem. Theory Comput.* **2019**, *15*, 3591–3609.

- (22) Sun, Q.; Berkelbach, T. C.; Blunt, N. S.; Booth, G. H.; Guo, S.; Li, Z.; Liu, J.; McClain, J. D.; Sayfutyarova, E. R.; Sharma, S.; Wouters, S.; Chan, G. K.-L. PySCF: the Python-based simulations of chemistry framework. *Wiley Interdiscip. Rev. Comput. Mol. Sci.* **2018**, *8*, e1340.
- (23) Thøgersen, L.; Olsen, J. coupled cluster and full configuration interaction study of CN and CN-. *Chem. Phys. Lett.* **2004**, *393*, 36–43.
- (24) Chan, G. K.-L.; Kállay, M.; Gauss, J. State-of-the-art density matrix renormalization group and coupled cluster theory studies of the nitrogen binding curve. *J. Chem. Phys.* **2004**, *121*, 6110–6116.
- (25) Helgaker, T.; Klopper, W.; Koch, H.; Noga, J. Basis-set convergence of correlated calculations on water. *J. Chem. Phys.* **1997**, *106*, 9639–9646.
- (26) Noga, J.; Bartlett, R. J. Coupled cluster calculations. *J. Chem. Phys.* **1987**, *86*, 7041, Erratum: *J. Chem. Phys.* **1988**, *89*, 3401.
- (27) Scuseria, G. E.; Schaefer, H. F. A new implementation of the full CCSDT model for molecular electronic structure. *Chem. Phys. Lett.* **1988**, *152*, 382–386.
- (28) Watts, J. D.; Bartlett, R. J. Correlation effects in quantum chemistry. *J. Chem. Phys.* **1990**, *93*, 6104.
- (29) Oliphant, N.; Adamowicz, L. New developments in coupled-cluster theory. *J. Chem. Phys.* **1991**, *95*, 6645.
- (30) Kucharski, S. A.; Bartlett, R. J. Higher-order correlation effects. *J. Chem. Phys.* **1992**, *97*, 4282.
- (31) Mejia-Rodriguez, D.; Aprà, E.; Autschbach, J.; Bauman, N. P.; Bylaska, E. J.; Govind, N.; Hammond, J. R.; Kowalski, K.; Kunitsa, A.; Panyala, A.; Peng, B.;

- Rehr, J. J.; Song, H.; Tretiak, S.; Valiev, M.; Vila, F. D. NWChem: Recent and Ongoing Developments. *J. Chem. Theory Comput.* **2023**, *19*, 7077–7096.
- (32) Cleland, D.; Booth, G. H.; Alavi, A. Communications: Survival of the fittest: Accelerating convergence in full configuration-interaction quantum Monte Carlo. *J. Chem. Phys.* **2010**, *132*, 041103.
- (33) Petruzielo, F. R.; Holmes, A. A.; Changlani, H. J.; Nightingale, M. P.; Umrigar, C. J. Semistochastic projector Monte Carlo method. *Phys. Rev. Lett.* **2012**, *109*, 230201.
- (34) Blunt, N. S.; Smart, S. D.; Kersten, J. A. F.; Spencer, J. S.; Booth, G. H.; Alavi, A. Semi-stochastic full configuration interaction quantum Monte Carlo: Developments and application. *J. Chem. Phys.* **2015**, *142*, 184107.